MESSENGER X-ray observations of magnetosphere–surface interaction on the nightside of Mercury

S.T. Lindsay [a,*], M.K. James [a], E.J. Bunce [a], S.M. Imber [a,b], H. Korth [c], A. Martindale [a], T.K. Yeoman [a]

[a] University of Leicester, Department of Physics & Astronomy, University Road, Leicester LE1 7RH, UK
[b] Department of Atmospheric, Oceanic and Space Sciences, University of Michigan, Ann Arbor, MI, USA
[c] Johns Hopkins University Applied Physics Laboratory, Laurel, MD, USA

ABSTRACT

The recently completed MESSENGER mission to Mercury has detected X-ray fluorescence events on the nightside surface of the planet, induced by the precipitation of electrons. We expand upon previously reported catalogues of such events, using a filter based on elemental fluorescence lines to construct a catalogue covering the full five years of the MESSENGER mission. We find that the locations of the majority of these events are ordered in two clear latitudinal bands on the dawn side of the planet centred at ∼50°N and ∼20°S. Electron precipitation is implied to be either stable or occurring repeatedly on timescales of up to several minutes, long in relation to characteristic times of the Mercury magnetospheric environment. Conversely, X-ray fluorescence events are observed on only ∼40% of MESSENGER orbits, although we note that some events are inevitably lost during the filtering process. We suggest that the regions of most intense precipitation are determined by the location of the relevant magnetic field line footprints on the surface. We are able to place speculative limits on the energies of electrons precipitating in this manner based on fluorescence lines in the observed X-ray spectra. The poleward boundaries of the regions of most intense precipitation are found to be collocated with the open-closed field line boundary. We use a magnetic field model to trace field lines from these fluorescence sites to implied locations of origin in the magnetotail.

© 2016 The Authors. Published by Elsevier Ltd. This is an open access article under the CC BY license (http://creativecommons.org/licenses/by/4.0/).

1. Introduction

The MESSENGER (MErcury Surface, Space ENvironment, GEochemistry, and Ranging) spacecraft was launched in August 2004 and achieved Mercury orbit on 18 March 2011 (Solomon et al., 2007). The orbital mission at Mercury lasted four years, before the spacecraft impacted the planetary surface on 30 April 2015. During this time, significant advances have been made in our understanding of Mercury's environment.

MESSENGER's orbit was highly elliptical, with periapsis ($h_p = 200$–500 km) at low altitude over the north pole and apoapsis high above the southern hemisphere ($h_a = 15\,000$ km, $\tau = 12$ h or $h_a = 12\,750$ km, $\tau = 8$ h dependent upon mission phase).

The MESSENGER X-Ray Spectrometer (XRS) was an X-ray fluorescence spectrometer consisting of three gas proportional counter (GPC) detectors (Schlemm et al., 2007), using a balanced filter method (Adler et al., 1972a,b) to separate the Kα fluorescence lines of the major rock-forming elements Mg (1.25 keV), Al (1.49 keV) and Si (1.74 keV). One GPC (GPC1-Mg) was equipped with a 4.5 µm Mg filter, the second (GPC2-Al) with a 6.3 µm Al filter, and the third (GPC3-UN) was unfiltered. The Mg and Al K-shell absorption edges (1.30 keV and 1.56 keV respectively) cause significant absorption within the respective filters across a small energy range. The differences between the spectra recorded by each of the three GPCs can thus be used to separate these three fluorescence lines.

XRS was nominally nadir-pointing with a 12° hexagonal field of view (FOV) with a triangular transmission function as a function of off-axis angle. XRS was paired with the Solar Assembly for X-rays (SAX), a solar monitor consisting of a Si PIN diode mounted on the spacecraft sunshield, used to monitor the incident X-ray spectrum (Schlemm et al., 2007).

Results from MESSENGER orbital operations in 2011 included the detection of X-ray fluorescence taking place on the nightside surface of Mercury (Starr et al., 2012), which was attributed to the impact of energetic particles on the planetary surface. Starr et al. (2012) characterises the illuminating particles as electrons with a kappa distribution in energy peaking at $0.8 < E < 1.4$ keV, and demonstrates sensitivity to the composition of the surface, producing elemental

---

abundance estimates for Mg, Al, S and Ca. Here, we extend the catalogue of nightside fluorescence events to cover the whole mission and discuss the location of the fluorescence sites and the implications for processes within Mercury's magnetic field.

2. Identification and characterisation of surface sites of electron-induced fluorescence

The existing catalogue of nightside electron-induced fluorescence events in 2011 was presented by Starr et al. (2012), who do not state how the events in question were identified. We have developed an automated filter to isolate candidate events over the full MESSENGER mission from March 2011 to April 2015, based on the detection of Si and/or Ca-Kα fluorescence from the unlit planetary surface. This filter applies a series of criteria to each XRS calibrated data record (CDR) as follows:

1. Rejects records with a low total count rate at any of the three GPCs ($< 2\ s^{-1}$ over whole spectrum).
2. Uses a peak finder (Dimeo, 2004) to check that there are more than zero peaks in the GPC spectrum. If no peaks are found, record is rejected.
3. Attempts a least-squares fit of a Gaussian curve to the GPC3 spectrum at 1.74 keV (Si-Kα).
4. If fitted peak has a maximum in the range $1.5 < E < 1.95$ keV, a width in the range $0.9 < \text{FWHM} < 1.4$ keV and a coefficient of determination $R^2 > 0.8$ (all criteria are selected empirically), then record is flagged as containing Si fluorescence.
5. If record is flagged, attempts to fit a peak to the GPC3 spectrum at 3.69 keV (Ca-Kα).
6. If fitted peak has a maximum in the range $3.4 < E < 3.8$ keV, a width in the range $1.4 < \text{FWHM} < 1.8$ keV and a coefficient of determination $R^2 > 0.9$ (all criteria are selected empirically), then record is flagged as containing Ca fluorescence.
7. If evidence exists of instrumental self-fluorescence in the Mg and Al filters (Mg/Al count rate at Mg/Al-filtered detector elevated above Mg/Al count rate at unfiltered detector) record is unflagged for both Si and Ca fluorescence.
8. If telemetry point FOV_STATUS (available in XRS CDR telemetry) indicates the instrument footprint is sunlit or entirely off planet, record is unflagged for both Si and Ca fluorescence. This is done to reject both solar-induced X-ray fluorescence and observations from astrophysical X-ray sources.

Si fluorescence is an ideal criterion for the filtering process as the energy required to excite it is low, and Si is expected to be present on the surface in large quantities with a near-isotropic distribution across the planet (Weider et al., 2015).

As described above we also produced a second catalogue based on the detection of Ca-Kα fluorescence in order to isolate events in which the illuminating flux is implied to contain a higher energy component. As with Si, Ca should be ubiquitous on the surface of the planet, with the average Ca/Si ratio being around 0.15, although more variation in Ca concentration is expected (Weider et al., 2015).

Fig. 1 shows an example spectrum collected by XRS at 15:23 UTC on 4 June 2012, with an integration time of 40 s. This record was selected by both the Si and Ca fluorescence filters described above. The spectra in Fig. 1 have been smoothed using a top hat filter 23 bins ($\sim$880 eV) in width to match the energy resolution of 880 eV FWHM at the Fe-K line (Schlemm et al., 2007). The strong Ca peak at 3.7 keV can be seen at all three GPCs, along with the Mg/Al/Si peak complex at $\sim$1.2–1.8 keV, which is observed as a single peak due to the energy resolution of the instrument. While Mg and Al peaks at the Mg and Al filtered GPCs may be indicative
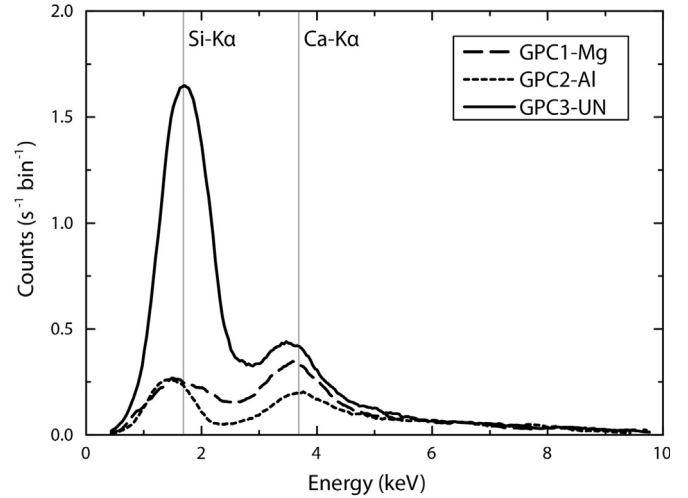

Fig. 1. Example XRS spectrum produced by electron-induced surface fluorescence, observed at 15:23 UTC on 4 June 2012; the original data have been smoothed using a top hat adjacent-averaging filter 23 bins in width. Si-Kα and Ca-Kα fluorescence energies are indicated.

of self-fluorescence, the presence of a strong peak at the unfiltered detector implies surface fluorescence, possibly from all three elements, although Si will usually be the strongest. Si/Mg/Al and Ca are not present in the unfiltered detector in areas vulnerable to self-fluorescence and thus we can be confident that their detection here is due to surface fluorescence.

Here we define a fluorescence "event" as made up of one or more contiguous "records" which are selected by the filter. Each record represents a single XRS integration time, which can vary between a minimum of 20 s and a maximum of 450 s depending on orbit and solar activity. Each event can be several records long, although the length of an event in terms of records does not necessarily reflect its length in time due to this wide variation in integration time.

The timestamps of records in the Si- and Ca-filtered electron-induced fluorescence catalogues were used as inputs to an analysis in SPICE (Acton, 1996), which retrieved the locations of the intersection of vectors describing the six corners of the XRS FOV, thus locating the region of the surface contributing to the observed fluorescence signal.

Subsequently, the spatial location of the XRS FOV on the planetary surface for each event was used as an input to a magnetic field model. A number of models of Mercury's magnetosphere exist (e.g. Luhmann et al., 1998; Sarantos et al., 2001; Korth et al., 2004; Alexeev et al., 2008). The magnetic field model used in this study is the KT14 model (Korth et al., 2015). The KT14 model consists of a number of modules, much like its counterparts made for Earth's magnetosphere (e.g. Tsyganenko, 1995, 2002a,b, 2013; Tsyganenko and Sitnov, 2005). The magnitude and morphology of each of the modules, or field sources, has been determined empirically and contained within a realistic magnetopause (Shue et al., 1997; Johnson et al., 2012). The KT14 model enables the tracing of field lines into the magnetotail without encountering unrealistic O-lines (Korth et al., 2014) like those which are found in the paraboloid model of Alexeev et al. (2008). This allows us to map events observed in the magnetosphere along field lines to the surface of Mercury, or from Mercury to a location within the magnetosphere – such as the magnetic equatorial plane.

The KT14 model was used to trace the implied magnetic field line associated with each fluorescence event back from its magnetic footprint (assumed to be collocated with the intersection of the XRS boresight with the planetary surface at the time of the event) to the magnetic equator. This analysis assumes that the

fluorescence event took place in the centre of the footprint, and that it was produced by electrons associated with a magnetic field line with a gyroradius which is small relative to the size of the XRS footprint; the latter assumption is reasonable given that gyroradii of electrons in the energy range considered will be of the order 1 km given a surface magnetic field strength of 200 nT. Protons and heavier ions are not considered for reasons discussed further in Section 3.1.

3. Results and discussion

When extended to cover the primary and extended MESSENGER mission from March 2011 to April 2015, our catalogue consists of 2048 fluorescence events, each consisting of one or more consecutive XRS records. In total the catalogue contains 3337 separate XRS records occurring during 1259 separate orbits, i.e. during approximately 40% of orbits with one or more records that satisfy the pointing condition. The longest duration event in terms of time is 2200 s (and 12 consecutive XRS records) long, while the longest in terms of contiguous XRS records is 18 records (and 360 s) long. We specify the length in both records and time because of the variable integration time of XRS; note that these two maxima do not refer to the same event. The low spatial resolution and long integration times mean that it is not possible to definitively state whether the start and end of any specific fluorescence event represent the start and end of a particle precipitation event or the movement of the instrument FOV over a region in which precipitation is ongoing.

It is not practical to include the full catalogue here (for which see supporting material). Table 1 summarises the frequency of events by length in records and time, and (for events more than one record in duration) by the range in latitude covered (the difference between the latitudes at the centre of the footprint for the first and last record in the event).

For the nine months (March–December 2011) over which the analysis presented here overlaps with the period considered by Starr et al. (2012), the filter developed for this work selects many more XRS records. Our filter selects 560 XRS records as opposed to 102 records identified over the same time period by Starr et al. (2012). Of the 99 nightside records included in the catalogue presented by Starr et al. (2012), 84 are replicated in our catalogue.

The remaining 15 records in the Starr catalogue immediately precede and/or follow records identified in our catalogue and probably represent continuations of the same fluorescent event. The only discrete events in the Starr catalogue not replicated here are from two events on 3 and 6 May 2011 during which the instrument footprint was lit by the Sun and are thus excluded by our filter.

The Ca-filtered event list is significantly shorter, consisting of 158 fluorescence events composed of 200 individual XRS records and occurring during 124 separate orbits (3.9%). Comparison with the Si-filtered catalogue therefore suggests that electron flux at or above the Ca K-edge (4.04 keV) is approximately an order of magnitude less frequent than flux at or above the Si K-edge (1.84 keV). The longest Ca-filtered event in time is 900 s (and 2 XRS records) long, while the longest in contiguous XRS records is 5 records (and 500 s) long. The Ca-filtered catalogue replicates 23 of the 102 XRS records listed in the Starr catalogue (which due to the filtering conditions described above are also replicated in the Si-filtered catalogue).

We are therefore able to place some limits on the stability of such events in time. Several fluorescence events are continuous over relatively long timescales (19 events exceed 15 min in duration) with respect to the short characteristic timescales of the Mercury magnetospheric system, with a Dungey cycle time of ~ 2 min (Slavin et al., 2010). However, we note that several individual instances of precipitation could be observed as a single fluorescence event, as the long (20–450 s) XRS integration time means the time resolution of these measurements is poor.

3.1. Identification of the fluorescing agent

As the events under discussion occur on the nightside of Mercury, direct illumination by solar X-rays can be immediately eliminated as a possible exciting source. Instead, it seems reasonable to presume that illumination by particles within the local environment must be responsible. X-ray fluorescence can be induced by any process which leads to inner shell ionisation of atoms within the target (i.e. the planetary surface). On the nightside surface of Mercury, we can limit the possible processes to electron, proton, or heavier ion impact, the most probable being electrons. For proton impact, the K-shell ionisation cross-section of a target is much smaller at low energies; therefore, the required proton energy to stimulate X-ray emission is much higher than that of electrons. For example, the cross-section of Si for electrons of 3.5 keV energy is approximately 8×10^{-25} m^2; the same cross-section for proton impact implies an energy of ~ 800 keV. Protons of the required energy would have large gyroradii in the weak Mercury magnetic field (> 1000 km at a local field strength of 50 nT and 90° pitch angle). Such a large gyroradius means that these particles are more likely to be lost to the solar wind from the magnetotail and are less likely to appear in groups precipitating at the planetary surface. Furthermore, protons above the 25 keV detection threshold of the EPS instrument have not been observed in the Mercury magnetosphere (Ho et al., 2011a). The same argument applies, to an even greater extent, to heavier ions such as Na$^+$, which have energies that have not been observed to exceed 13 keV (Raines et al., 2014), although modelling predicts Na$^+$ ions in the magnetotail with energies of up to 50 keV (Seki et al., 2013) – at which energies the ionisation cross-section remains negligibly low. Therefore, even were proton precipitation occurring, we could reasonably expect electron-induced X-ray fluorescence to dominate, meaning electrons become the most likely source of these fluorescence events. This is consistent with the findings of Starr et al. (2012) and the observations of suprathermal electrons by Ho et al. (2011b) and Schriver et al. (2011).
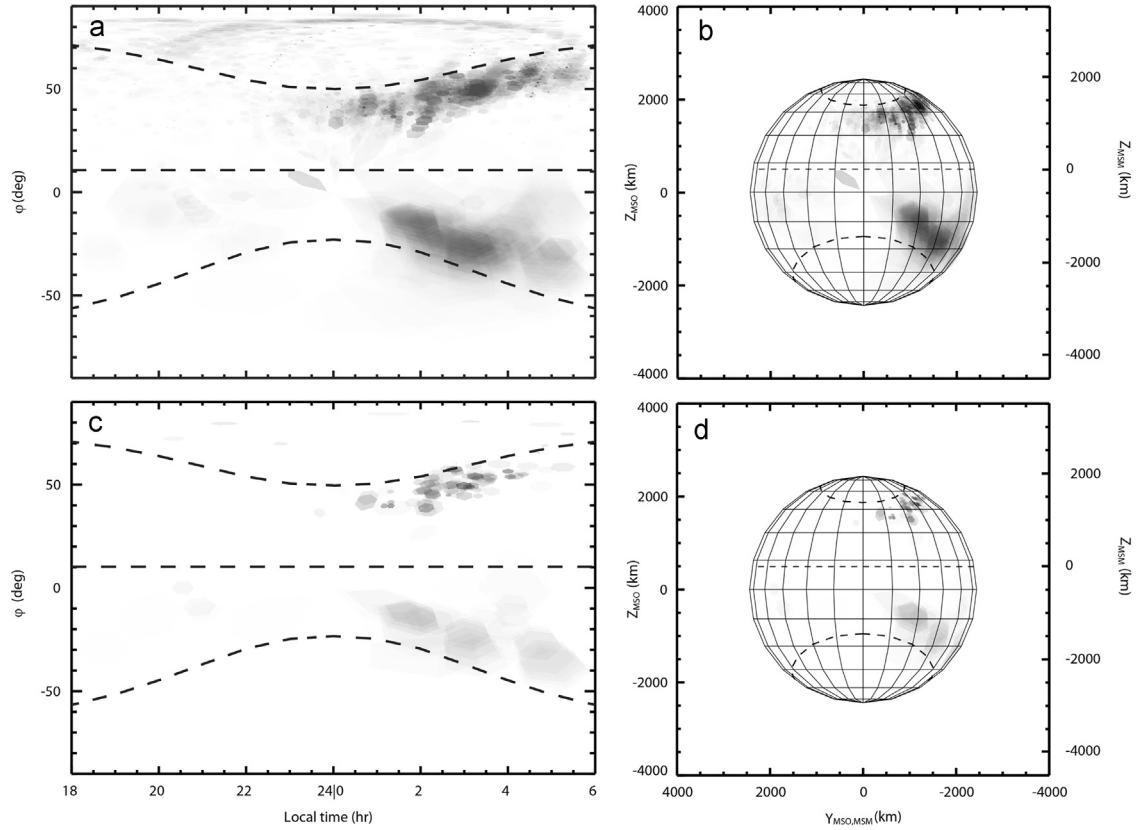
Table 1
Descriptive statistics of catalogues of nightside Si-Kα and Ca-Kα fluorescence events. Note that the latitude range column excludes events that are one record long.

Length (records)	N_{Si}	N_{Ca}	Length (s)	N_{Si}	N_{Ca}	Latitude range (deg)	N_{Si}	N_{Ca}
1	1474	126	0–125	1420	137	0–3	190	16
2	288	25	126–250	430	46	3–6	164	8
3	127	5	251–375	23	3	6–9	95	1
4	74	1	376–500	101	11	9–12	41	3
5	29	1	501–625	40	2	12–15	24	1
6	31	0	626–750	1	0	15–18	20	1
7	6	0	751–875	12	0	18–21	11	2
8	7	0	876–1000	2	1	21–24	10	0
9	0	0	1001–1125	3	0	24–27	4	0
10	3	0	1126–1250	7	0	27–30	2	0
11	1	0	1251–1375	3	0	30–33	3	0
12	3	0	1376–1500	3	0	33–36	2	0
13	2	0	1501–1625	2	0	36–39	1	0
14	1	0	1626–1750	0	0	39–42	2	0
15	0	0	1751–1875	0	0	42–45	2	0
16	1	0	1876–2000	0	0	45–48	1	0
17	0	0	2001–2125	0	0	48–51	1	0
18	1	0	2125–2250	1	0	51–54	1	0

Fig. 2. Maps of XRS footprint locations associated with XRS records containing electron-induced surface fluorescence in (a) latitude–local time and (b) cartesian (Y–Z_{MSO} and Y–Z_{MSM}) coordinates. (c) and (d) show XRS footprint locations during events in which Ca is fluoresced in addition to Si. Grey scale indicates number of overlapping footprints, scaled by count rate and size of footprint. Dashed lines show location of magnetic equator and modelled open-closed field line boundary.

3.2. Surface mapping

Fig. 2 shows two projections of a map of XRS footprint locations, plotting the locations associated with each record containing electron-induced fluorescence as per both the Si-filtered (Fig. 2a and b) and Ca-filtered (Fig. 2c and d) catalogues. Footprints with one or more corners off the planet tend to be very large, and have been excluded for clarity. The grey scale on the maps represents the number of overlapping footprints at each location, scaled for both count rate and footprint size, acting as an indication of the frequency of fluorescence-inducing electron precipitation at these locations. In the southern hemisphere, where MESSENGER orbited at high altitude, the XRS footprint is large and thus spatial resolution is low. Therefore there is increased error in the southern hemisphere in both surface location of each fluorescence event and in the estimation of precipitation frequency, as footprints are more likely to overlap and the integration time associated with each footprint is much longer. Dashed lines on each map show the location of the magnetic equator ($Z_{MSO} = 484 \pm 11$ km, Anderson et al., 2011) and of the average open-closed field line boundary (OCB) predicted by the magnetic field model of Korth et al. (2015), discussed further in Section 3.4. Fig. 2b and d uses the Mercury Solar Orbital (MSO) and Mercury Solar Magnetospheric (MSM) reference frames, as defined within the relevant MESSENGER SPICE kernel (Turner and Nguyen, 2009), to project the same data. In the MSO frame, the origin is at the centre of Mercury, the x-axis is positive sunward, the y-axis is aligned with the Mercury orbital anti-velocity vector, and the z-axis makes up the right handed set and approximately coincides with the planetary spin axis. The MSM frame is identical except that the origin is displaced 484 km in the $+Z$ direction to account for the offset dipole.

The Si-filtered maps (Fig. 2a and b) show the locations of most frequent surface fluorescence. The most frequent electron precipitation at energies above the Si K-edge is found to be strongly asymmetric

about local midnight, but approximately symmetric about the magnetic equator. The distribution in latitude shows two well-defined bands in the north and south, the poleward boundaries of which align closely with the model OCB. The northern band is located in latitude from approximately $35°$ to $65°$N and extends from 0 h to 6 h local time, although the boundary at 6 h may be imposed by the terminator as records with footprints located here will no longer satisfy the filter conditions. It is skewed from horizontal so that it shifts poleward as local time increases. The band is approximately constant in width, at 10–$15°$ latitude. The southern band, though more diffuse and variable in width (presumably due to observation effects, e.g. larger instrument footprints), likewise extends across the same range in local time and moves poleward with increasing local time. It is not possible to determine to what extent the north–south asymmetry in the shape and extent of these regions is real as opposed to an effect of the asymmetry in footprint size, and so we do not comment further on this asymmetry here, although a similar asymmetry is expected given the offset dipole. The shorter catalogue formed from events containing higher energy fluorescence at the Ca line, when plotted in like manner, produces footprints in a very similar pattern (Fig. 2c and d).

A frequency histogram of the Si-filtered boresight locations in latitude (Fig. 3a) shows the two groups clearly; the southern group with a maximum at $\sim 20°$S and the northern group with a maximum at $\sim 50°$N, or $\sim 31°$ and $\sim 39°$ north and south of the magnetic equator respectively. A similar histogram in local time (Fig. 3b) shows the strong dawn–dusk asymmetry, with the highest frequency of events occurring at a local time of approximately 03:00. Fig. 3c and d shows histograms of the same locations for the Ca-filtered fluorescence catalogue.

We cannot exclude the possibility that some records that have been rejected due to evidence of instrumental self-fluorescence could also contain evidence of surface fluorescence. The processes inducing these two sources of fluorescence are not mutually exclusive; therefore, a
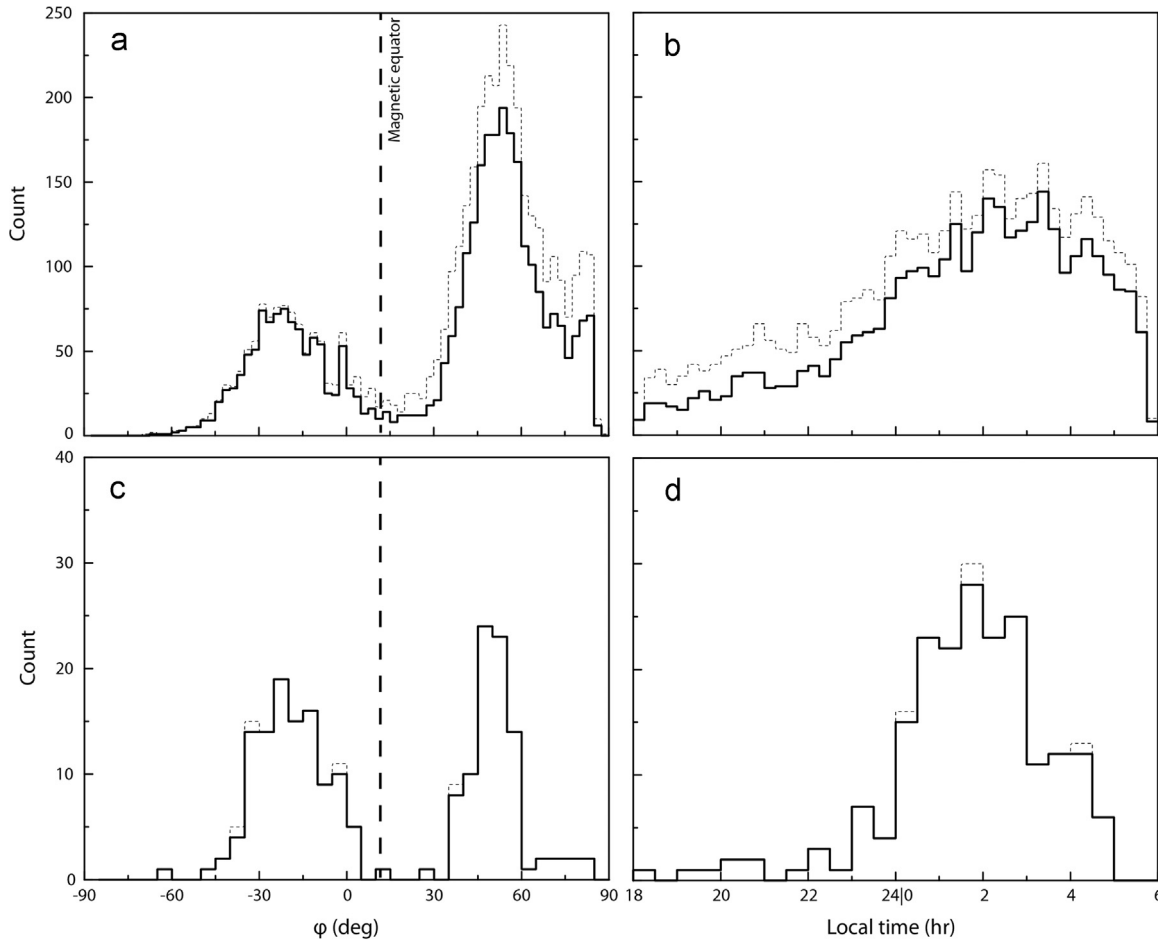
Fig. 3. (a) Histogram of nightside Si surface fluorescence events by location of boresight vector in latitude ϕ; the location of the magnetic equator is shown. (b) Histogram of nightside Si surface fluorescence events by location of boresight vector in local time. Dashed lines represent the same histograms if records containing instrumental self-fluorescence are not filtered from the dataset. (c) and (d) are histograms of the same for Ca fluorescence events.

dashed line shows the same histograms if no filtering for self-fluorescence is conducted. It is clear that the inclusion of self-fluorescence events would not significantly alter the conclusions of this work.

It is important to note that spacecraft coverage of the nightside surface is symmetric about local midnight, and the coverage of the dusk side of the planet is comparable to that of the dawn side; that is, the observed asymmetry in event locations is not a result of an asymmetry in the surface coverage.

Coverage is also mostly symmetrical north–south, and hence the observed northern and southern boundaries are independent of coverage, with the exception of the poleward boundary of the southern grouping ($\sim$50°S). Southward of this latitude, the XRS footprint becomes very large, covering most of the planetary surface and also including deep space (and so the footprints are excluded from the above plots). For this reason, it is difficult to definitively identify the southern boundary of this grouping as real (and thus probably associated with the southern OCB).

We see no significant seasonal trend in the frequency of fluorescence events, although we note that, given the nature of this data set, it is not possible to isolate real seasonal variation due to effects such as solar activity, reconnection rate or solar wind forcing from other effects that may be expected to vary with the same or similar period, including the rotation in the plane of MESSENGER's orbit, the XRS integration time, and instrument temperature.

Walsh et al. (2013) use the magnetic field model of Alexeev et al. (2008, 2010) to predict the trajectories of 34 keV electrons

injected at the magnetic equator at local midnight with start positions in the range $-1.05R_M > X_{MSM} > -1.65R_M$ and an isotropic pitch angle distribution from 0° to 180°. Of the modelled electrons which precipitate at the surface, the distribution in latitude is very similar to that observed in the nightside fluorescence events found in this study. Fig. 4 reproduces the latitude histogram of fluorescence event locations from Fig. 3a in grey, with the histogram of predicted electron precipitation events from Walsh et al. (2013) overlaid in black. The locations of both distributions are very similar, but the intensities and widths vary; in particular, the observed relative intensities in north and south are opposite to those predicted. Note, however, that the nature of the XRS catalogue discussed here means that neither of these quantities are described well in the southern hemisphere. Furthermore, the energy of the electrons inducing the nightside fluorescence events is only required to be above 1.84 keV (the Si K-edge), as opposed to the modelled electrons which have a much higher energy of 34 keV. Walsh et al. (2013) do not discuss the distribution of the modelled precipitation of electrons in local time.

3.3. Frequency and duration of events

Electron precipitation, at least at energies above the Si K-edge, does not appear to be a steady-state process as it is observed during only $\sim$40% of MESSENGER orbits where pointing conditions are satisfied. Conversely, we observe events over several consecutive XRS records, which imply prolonged precipitation over timescales of several minutes or separate events taking place

within the same integration period. Obviously, it is not possible using this technique to detect electron precipitation at energies below the lower detection threshold of XRS, and we therefore

cannot speculate on the frequency (or otherwise) of electron precipitation below this threshold, but it is not unreasonable to propose that it may be present.
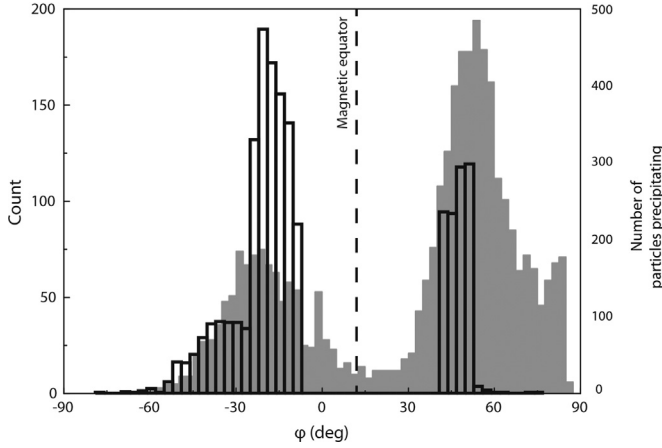
3.4. Magnetic field modelling

Fig. 5 shows the field lines traced from the locations of the events in the Ca-filtered catalogue which lie north of the magnetic equator – the shorter data set is used for clarity. As Fig. 3 shows, the distribution in location in the Ca-filtered catalogue is representative of the distribution of the Si-filtered catalogue. Fig. 5 also shows a heat map of the locations of the intersection with the magnetic equator of the field lines traced from the locations of all events in the Si catalogue where these field lines are closed (as open field lines will not intersect the equator). This represents the exclusion of 11.5% of events in the north and 18.1% of events in the south. These figures use the MSM coordinate system described in Section 3.2.

The OCB predicted by this model lies along the poleward boundaries of the strongest groupings of the observed fluorescence events, and the majority (72%) of the locations of fluorescence events map to closed rather than open magnetic field lines. The fluorescence events which take place in the open field line region do not exhibit any clear spatial distribution compared to
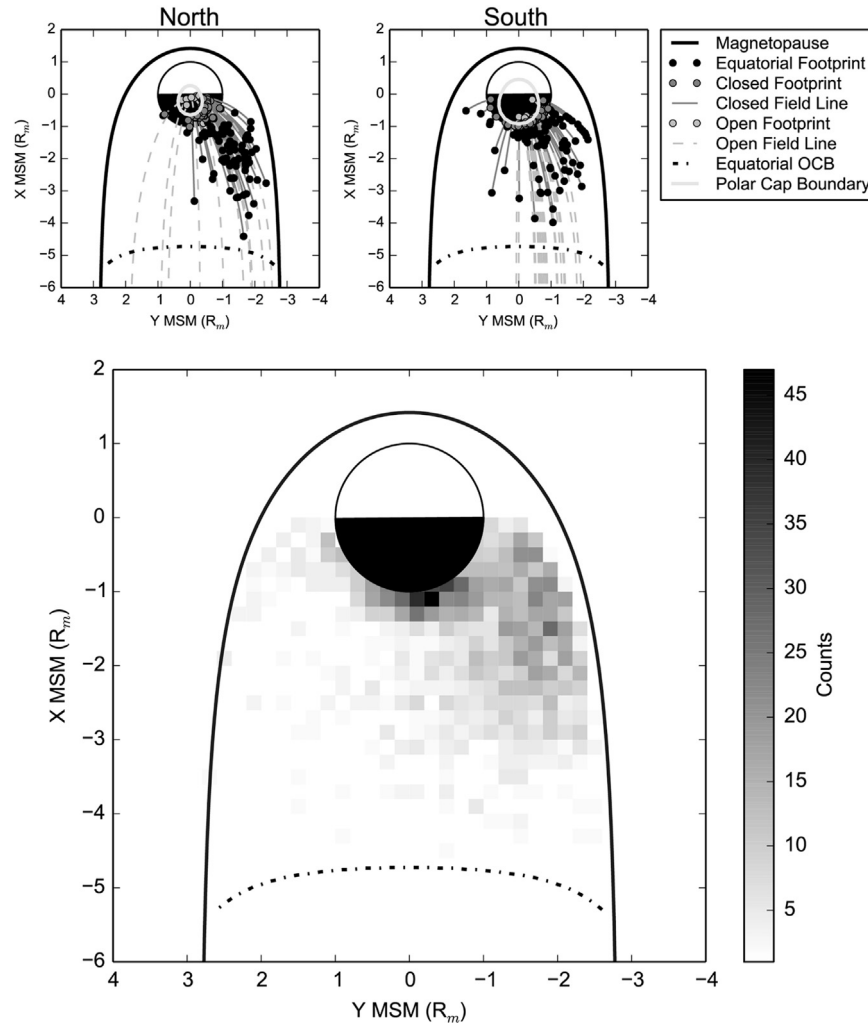
Fig. 4. Plotted in grey is a histogram of Si-filtered nightside surface fluorescence events by location of XRS boresight vector in latitude ϕ; overlaid in black is a histogram of predicted locations of precipitation for 34 keV electrons injected at the antisunward equator, from Walsh et al. (2013).

Fig. 5. (Top) Plot in X–Y_{MSM} space of locations of surface fluorescence events with associated field lines from an average magnetic field model. Surface events are the events in the Ca filtered catalogue; left panel shows events taking place in the northern hemisphere, right panel those in the southern hemisphere. Solid dark grey lines represent closed magnetic field lines, while dashed light grey lines are open. Dark grey dots indicate equatorial footprints. Solid black line indicates the magnetopause, dotted black line the equatorial OCB. (Bottom) Heat map in X–Y_{MSM} space of equatorial footprints associated with each event.

those within the boundary. We note that due to the short time-scales of processes within the Mercury magnetosphere and the comparatively long integration time of XRS, field lines that are open in the average model may have been closed during some part of the associated fluorescence event. Fig. 5 shows that the great majority of closed field line events originate within the dawnside magnetotail. Very few of the field lines extend as far as the equatorial OCB (shown as dotted lines in Fig. 5), although this is does not rule out the interpretation that electron injection occurs at reconnection sites in the tail, since the newly closed field lines will convect rapidly planetward on timescales comparable to the integration time of XRS.

Anderson et al. (2014) report Region 1 like field-aligned currents observed near the poles, detected through magnetic field perturbations in magnetometer data. As at Earth, these are aligned such that electrons flow towards the planet on the duskside and away from the planet on the dawnside. A Region 2-polarity current, which would be of opposite polarity and lie equatorward of Region 1 (e.g. Iijima and Potemra, 1978), would therefore involve the flow of electrons toward the planet on the dawnside. Anderson et al. (2014) do not observe a Region 2-like current in the magnetic field data, and speculate that "plasma convecting sunward from the nightside magnetosphere may impact Mercury's surface before it produces [Region 2] currents". The results presented here provide support for this idea, with electrons of energy above 1.8 keV precipitating at the dawnward surface. However, we note that particles forming a true Region 2 current may be of too low an energy to be detected by this method, and these results do not preclude the existence of such a current.

The results from our analysis support the conclusion that energetic electrons accelerated in the tail at a near-Mercury X-line are trapped on closed plasma sheet field lines. These lines convect sunward in a gradient-curvature drift process somewhat similar to that seen at Earth and other magnetised planets in the formation of the ring current, while electrons preferentially drift towards local dawn. A recent study by Baker et al. (2015) has provided evidence that electrons in a narrow energy band may complete a full drift orbit; however the majority of electrons that generate the observed X-ray fluorescence must have greater energies and therefore precipitate onto the planetary surface. Such a process could produce the pattern we observe – the dawn–dusk asymmetry being due to the drift of electrons towards dawn and protons towards dusk. Some proton-induced fluorescence at dusk may be expected, but at a much lower level than electron-induced fluorescence. The distribution in latitude simply reflects the areas in which closed magnetic field lines intersect the surface – the poleward boundary represents the projection of the open-closed field line boundary onto the planetary surface. Precipitation does occur in the open field line region as well as on the dusk side of the planet, but this is both less frequent and without apparent ordering. Due to the short timescales associated with processes in the Mercury magnetosphere, the process we describe would be completed rapidly – e.g. 2–4 minutes (Walsh et al., 2013; Baker et al., 2015) – and thus the longer events in our catalogue may represent multiple serial occurrences of the reconnection–convection–precipitation process that occur within a single XRS integration time.

4. Conclusions

We have discussed the development of a filter which identifies the locations of electron-induced fluorescence on the nightside surface of Mercury, extending the analysis described by Starr et al. (2012). These locations, when plotted on the planetary surface in latitude–local time space, form clear groupings which are strongly asymmetric in local time (dusk–dawn) and strongly symmetric in latitude about the magnetic equator. The location of the fluorescence events in latitude agrees well with electron precipitation predictions made by Walsh et al. (2013) for electrons injected at the nightside magnetic equator.

Using a magnetic field model derived from that of Korth et al. (2015) we have tracked the implied origin site for the precipitating electrons assuming motion along magnetic field lines. The origin sites are concentrated in the dawnside magnetotail. The majority of the events track to closed field lines, with the northern open-closed field line boundary estimated by the model aligning closely with the northern boundary of fluorescence events on the surface.

Fluorescence events are only detected during some 40% of MESSENGER orbits. The events are therefore not generated by a steady-state process, but where events are not detected it is not possible to determine whether this is due to a simple absence of precipitating electron flux or due to a precipitating flux with energies too low to excite Si fluorescence in the surface. The latter scenario is supported, although indirectly and not conclusively, by the steep electron energy spectrum implied by the greatly lower incidence of events containing Si and Ca fluorescence versus those containing Si fluorescence alone.

The observed regions of intense electron-induced surface fluorescence are consistent with the interpretation of Anderson et al. (2014), who detect Region 1 polarity currents using magnetometer data, but suggest that no Region 2-like current is observed because plasma convecting sunward from the nightside impacts the surface of the planet before producing a Region 2 current. Ho et al. (2011b) and Lawrence et al. (2015) have described the detection of 1–10 keV electrons on closed field lines within the magnetosphere using XRS and the MESSENGER neutron spectrometer respectively, which may represent observations of the same population before they reach the planetary surface and precipitate.

The ESA/JAXA BepiColombo Mercury orbiter (Benkhoff et al., 2010), which will be operating at Mercury in 2024–2025, and MIXS, the imaging X-ray spectrometer on board (Fraser et al., 2010) will be able to address some of these open questions. The BepiColombo MPO orbit is much lower in altitude in the southern hemisphere than MESSENGER's, and is symmetric about the planetary equator, allowing better characterisation of the location of surface fluorescence events in the south. MIXS will be able to observe the same fluorescence events, but can also detect O-Kα and Fe-Lα fluorescence at 525 eV and 705 eV respectively. It will therefore be able to detect fluorescence even when the energy of the precipitating electron flux does not exceed the Si K-edge, which will allow us to make a much more complete characterisation of the energy spectrum of the electron population. Furthermore, the Mercury Electron Analyzer, part of the Mercury Plasma Particle Experiment (Saito et al., 2010) suite of instruments on board BepiColombo MMO, will be able to directly detect eV to keV energy electrons, allowing much more complete characterisation of the electron environment near Mercury.

Appendix A. Supplementary data

Supplementary data associated with this paper can be found in the online version at http://dx.doi.org/10.1016/j.pss.2016.03.005.

References

Acton, C.H., 1996. Ancillary data services of NASA's navigation and ancillary information facility. Planet. Space Sci. 44 (1), 65–70.

Adler, I., Trombka, J.I., Gerard, J., Lowman, P., Schmadebeck, R., Blodget, H., Eller, E., Yin, L., Lamothe, R., Gorenstein, P., Bjorkholm, P., 1972a. Apollo 15 geochemical X-ray fluorescence experiment: preliminary report. Science 175, 436–440.

Adler, I., Trombka, J.I., Gerard, J., Lowman, P., Schmadebeck, R., Blodget, H., Eller, E., Yin, L., Lamothe, R., Osswald, G., Gorenstein, P., Bjorkholm, P., Gursky, H., Harris, B., 1972b. Apollo 16 geochemical X-ray fluorescence experiment: preliminary report. Science 177, 256–259.

Alexeev, I.I., Belenkaya, E.S., Bobrovnikov, S.Y., Slavin, J.A., Sarantos, M., 2008. Paraboloid model of Mercury's magnetosphere. J. Geophys. Res. 113.

Alexeev, I.I., Belenkaya, E.S., Slavin, J.A., Korth, H., Anderson, B.J., Baker, D.M.H., Boardsen, S.A., Johnson, C.L., Purucker, M.E., Sarantos, M., Solomon, S.C., 2010. Mercury's magnetospheric magnetic field after the first two MESSENGER fly-bys. Icarus 209, 23–39.

Alexeev, I.I., Belenkaya, E.S., Yu. Bobrovnikov, S., Slavin, J.A., Sarantos, M., 2008. Paraboloid model of Mercury's magnetosphere. J. Geophys. Res.: Space Phys. 113 (A12), a12210. http://dx.doi.org/10.1029/2008JA013368.

Anderson, B.J., Johnson, C.L., Korth, H., Purucker, M.E., Winslow, R.M., Slavin, J.A., Solomon, S.C., McNutt, R.L., Raines, J.M., Zurbuchen, T.H., 2011. The global magnetic field of Mercury from MESSENGER orbital observations. Science 333, 1859–1862.

Anderson, B.J., Johnson, C.L., Korth, H., Slavin, J.A., Winslow, R.M., Phillips, R.J., McNutt, R.L., Solomon, S.C., 2014. Steady-state field aligned currents at Mercury. Geophys. Res. Lett. 41, 7444–7452.

Baker, D.N., Dewey, R., Anderson, B.J., Ho, G.C., Korth, H., Krimigis, S.M., Lawrence, D.J., McNutt, R.L., Odstrcil, D., Raines, J.M., Schriver, D., Slavin, J.A., Solomon, S.C., 2015. Energetic electron flux enhancements in Mercury's magnetosphere: an integrated view with multi-instrument observations from MESSENGER. Geophys. Res. Abstr. 17, 2517.

Benkhoff, J., van Casteren, J., Hayakawa, H., Fujimoto, M., Laakso, H., Novara, M., Ferri, P., Middleton, H.R., Ziethe, R., 2010. BepiColombo—comprehensive exploration of Mercury: mission overview and science goals. Planet. Space Sci. 58, 2–20.

Dimeo, R.M., 2004. GET_PEAK_POS. NIST Center for Neutron Research (URL ⟨http://www.ncnr.nist.gov/staff/dimeo/riddle/get_peak_pos.pro⟩).

Fraser, G.W., Carpenter, J.D., Rothery, D.A., Pearson, J.F., Martindale, A., Huovelin, J., Treis, J., Anand, M., Anttila, M., Ashcroft, M., Benkhoff, J., Bland, P., Bowyer, A., Bradley, A., Bridges, J., Brown, C., Bulloch, C., Bunce, E.J., Christensen, U., Evans, M., Fairbend, R., Feasey, M., Giannini, F., Hermann, S., Hesse, M., Hilchenbach, M., Jorden, T., Joy, K., Kaipiainen, M., Kitchingman, I., Lechner, P., Lutz, G., Malkki, A., Muinonen, K., Näränen, J., Portin, P., Prydderch, M., San Juan, J., Sclater, E., Schyns, E., Stevenson, T.J., Strüder, L., Syrjasuo, M., Talboys, D., Thomas, P., Whitford, C., Whitehead, S., 2010. The Mercury imaging X-ray spectrometer (MIXS) on BepiColombo. Planet. Space Sci. 58, 79–95.

Ho, G.C., Krimigis, S.M., Gold, R.E., Baker, D.N., Slavin, J.A., Anderson, B.J., Korth, H., Starr, R.D., Lawrence, D.J., McNutt, R.L., Solomon, S.C., 2011a. MESSENGER observations of transient bursts of energetic electrons in Mercury's magnetosphere. Science 333, 1865–1868.

Ho, G.C., Starr, R.D., Gold, R.E., Krimigis, S.M., Slavin, J.A., Baker, D.N., Anderson, B.J., McNutt, R.L., Nittler, L.R., Solomon, S.C., 2011b. Observations of suprathermal electrons in Mercury's magnetosphere during the three MESSENGER flybys. Planet. Space Sci. 59, 2016–2025.

Iijima, T., Potemra, T.A., 1978. Large-scale characteristics of field-aligned currents associated with substorms. J. Geophys. Res.: Space Phys. 83 (A2), 599–615. http://dx.doi.org/10.1029/JA083iA02p00599.

Johnson, C.L., Purucker, M.E., Korth, H., Anderson, B.J., Winslow, R.M., Al Asad, M.M. H., Slavin, J.A., Alexeev, I.I., Phillips, R.J., Zuber, M.T., Solomon, S.C., 2012. Messenger observations of Mercury's magnetic field structure. J. Geophys. Res.: Planets 117 (E12), e00L14. http://dx.doi.org/10.1029/2012JE004217.

Korth, H., Anderson, B.J., Acuña, M.H., Slavin, J.A., Tsyganenko, N.A., Solomon, S.C., McNutt, R.L., 2004. Determination of the properties of Mercury's magnetic field by the MESSENGER mission. Planet. Space Sci. 52 (8), 733–746 (URL ⟨http://www.sciencedirect.com/science/article/pii/S0032063304000133⟩).

Korth, H., Anderson, B.J., Gershman, D.J., Raines, J.M., Slavin, J.A., Zurbuchen, T.H., Solomon, S.C., McNutt, R.L., 2014. Plasma distribution in Mercury's magnetosphere derived from MESSENGER magnetometer and fast imaging plasma spectrometer observations. J. Geophys. Res.: Space Phys. 119 (4), 2917–2932. http://dx.doi.org/10.1002/2013JA019567.

Korth, H., Tsyganenko, N.A., Johnson, C.L., Philpott, L.C., Anderson, B.J., Al Asad, M. M., Solomon, S.C., McNutt, R.L., 2015. Modular model for Mercury's magnetospheric magnetic field confined within the average observed magnetopause. J. Geophys. Res.: Space Phys. 120 (6), 4503–4518. http://dx.doi.org/10.1002/2015JA021022.

Lawrence, D.J., Anderson, B.J., Baker, D.N., Feldman, W.C., Ho, G.C., Korth, H., McNutt, R.L., Peplowski, P.N., Solomon, S.C., Starr, R.D., Vandegriff, J.D., Winslow, R.M., 2015. Comprehensive survey of energetic electron events in Mercury's magnetosphere with data from the MESSENGER gamma-ray and neutron spectrometer. J. Geophys. Res.: Space Phys. 120 (4), 2851–2876.

Luhmann, J.G., Russell, C.T., Tsyganenko, N.A., 1998. Disturbances in Mercury's magnetosphere: are the Mariner 10 "substorms" simply driven?. J. Geophys. Res.: Space Phys. 103 (A5), 9113–9119. http://dx.doi.org/10.1029/97JA03667.

Raines, J.M., Gershman, D.J., Slavin, J.A., Zurbuchen, T.H., Korth, H., Anderson, B.J., Solomon, S.C., 2014. Structure and dynamics of Mercury's magnetospheric cusp: messenger measurements of protons and planetary ions. J. Geophys. Res.: Space Phys. 119 (8), 6587–6602. http://dx.doi.org/10.1002/2014JA020120.

Saito, Y., Sauvaud, J.A., Hirahara, M., Barabash, S., Delcourt, D., Takashima, T., Asamura, K., 2010. Scientific objectives and instrumentation of Mercury plasma particle experiment (MPPE) onboard MMO. Planet. Space Sci. 58 (1–2), 182–200.

Sarantos, M., Reiff, P.H., Hill, T.W., Killen, R.M., Urquhart, A.L., 2001. A Bx-interconnected magnetosphere model for Mercury. Planet. Space Sci. 49 (14–15), 1629–1635 (Returns to Mercury. URL ⟨http://www.sciencedirect.com/science/article/pii/S0032063301001003⟩).

Schlemm, C.E., Starr, R.D., Ho, G.C., Bechtold, K.E., Hamilton, S.A., Boldt, J.D., Boynton, W.V., Bradley, W., Fraeman, M.E., Gold, R.E., Goldsten, J.O., Hayes, J.R., Jaskulek, S.E., Rossano, E., Rumph, R.A., Schaefer, E.D., Strohbehn, K., Shelton, R. G., Thompson, R.E., Trombka, J.I., Williams, B.D., 2007. The X-ray spectrometer on the MESSENGER spacecraft. Space Sci. Rev. 131, 393–415.

Schriver, D., Trávníček, P., Anderson, B.J., Ashour-Abdalla, M., Baker, D.N., Benna, M., Boardsen, S.A., Gold, R.E., Hellinger, P., Ho, G.C., Korth, H., Krimigis, S.M., McNutt, R.L., Raines, J.M., Richard, R.L., Slavin, J.A., Solomon, S.C., Starr, R.D., Zurbuchen, T.H., 2011. Quasi-trapped ion and electron populations at Mercury. Geophys. Res. Lett. 38.

Seki, K., Terada, N., Yagi, M., Delcourt, D., Leblanc, F., Ogino, T., 2013. Effects of the surface conductivity and the imf strength on the dynamics of planetary ions in Mercury's magnetosphere. J. Geophys. Res.: Space Phys. 118 (6), 3233–3242. http://dx.doi.org/10.1002/jgra.50181.

Shue, J.-H., Chao, J.K., Fu, H.C., Russell, C.T., Song, P., Khurana, K.K., Singer, H.J., 1997. A new functional form to study the solar wind control of the magnetopause size and shape. J. Geophys. Res.: Space Phys. 102 (A5), 9497–9511. http://dx.doi.org/10.1029/97JA00196.

Slavin, J.A., Anderson, B.J., Baker, D.N., Benna, M., Boardsen, S.A., Gloeckler, G., Gold, R.E., Ho, G.C., Korth, H., Krimigis, S.M., McNutt, R.L., Nittler, L.R., Raines, J.M., Sarantos, M., Schriver, D., Solomon, S.C., Starr, R.D., Trávníček, P.M., Zurbuchen, T.H., 2010. MESSENGER observations of extreme loading and unloading of Mercury's magnetic tail. Science 329 (5992), 665–668.

Solomon, S.C., McNutt, R.L., Gold, R.E., Domingue, D.L., 2007. MESSENGER mission overview. Space Sci. Rev. 131, 3–39.

Starr, R.D., 2010. MESSENGER E/V/H XRS calibrated (CDR) spectra v1.0. NASA Planetary Data System.

Starr, R.D., Schriver, D., Nittler, L.R., Weider, S.Z., Byrne, P.K., Ho, G.C., Rhodes, E.A., Schlemm II, C.E., Solomon, S.C., Trávníček, P.M., 2012. MESSENGER detection of electron-induced X-ray fluorescence from Mercury's surface. J. Geophys. Res. 117, E00L02.

Tsyganenko, N.A., 1995. Modeling the Earth's magnetospheric magnetic field confined within a realistic magnetopause. J. Geophys. Res.: Space Phys. 100 (A4), 5599–5612. http://dx.doi.org/10.1029/94JA03193.

Tsyganenko, N.A., 2002a. A model of the near magnetosphere with a dawn–dusk asymmetry. 1. Mathematical structure. J. Geophys. Res.: Space Phys. 107 (A8). http://dx.doi.org/10.1029/2001JA000219 (SMP12-1–SMP12-15).

Tsyganenko, N.A., 2002b. A model of the near magnetosphere with a dawn–dusk asymmetry. 2. Parameterization and fitting to observations. J. Geophys. Res.: Space Phys. 107 (A8). http://dx.doi.org/10.1029/2001JA000220 (SMP10-1–SMP10-17).

Tsyganenko, N.A., 2013. Data-based modelling of the Earth's dynamic magnetosphere: a review. Ann. Geophys. 31 (10), 1745–1772 (URL ⟨http://www.ann-geophys.net/31/1745/2013/⟩).

Tsyganenko, N.A., Sitnov, M.I., 2005. Modeling the dynamics of the inner magnetosphere during strong geomagnetic storms. J. Geophys. Res.: Space Phys. 110 (A3), A03028. http://dx.doi.org/10.1029/2004JA010798.

Turner, S., Nguyen, L., 2009. MESSENGER Dynamic Frame Definitions Kernel. JHUAPL (URL ⟨http://naif.jpl.nasa.gov/pub/naif/pds/data/mess-e_v_h-spice-6-v1.0/messsp_1000/data/fk/msgr_dyn_v600.tf⟩).

Walsh, B.M., Ryou, A.S., Sibeck, D.G., Alexeev, I.I., 2013. Energetic particle dynamics in Mercury's magnetosphere. J. Geophys. Res.: Space Phys. 118, 1992–1999.

Weider, S.Z., Nittler, L.R., Starr, R.D., Crapster-Pregont, E.J., Peplowski, P.N., Denevi, B. W., Head, J.W., Byrne, P.K., Hauck, S.A., Ebel, D.S., Solomon, S.C., 2015. Evidence for geochemical terranes on Mercury: global mapping of major elements with MESSENGER's X-Ray Spectrometer. Earth Planet. Sci. Lett. 416, 109–120 (URL ⟨http://www.sciencedirect.com/science/article/pii/S0012821X15000448⟩).